Gigahertz nano-optomechanical resonances in a dielectric SiC-membrane metasurface array

Idris A. Ajia[1]*, Jun-Yu Ou[2], Nicholas J. Dinsdale[1], H. Johnson Singh[1], Theo Chen-Sverre[1], Tongjun Liu[2], Nikolay I. Zheludev[2, 3], and Otto L. Muskens[1]*

[1]Physics and Astronomy, Faculty of Physical Sciences and Engineering, University of Southampton, SO17 1BJ, Southampton, United Kingdom

[2]Optoelectronics Research Centre and Centre for Photonic Metamaterials, University of Southampton, Southampton, SO17 1BJ, United Kingdom

[3]Centre for Disruptive Photonic Technologies, School of Physical and Mathematical Sciences and The Photonics Institute, Nanyang Technological University, Singapore 637378, Singapore

Corresponding authors: o.muskens@soton.ac.uk, idris.ajia@soton.ac.uk

Abstract

Optically and vibrationally resonant nanophotonic devices are of particular importance for their ability to enhance optomechanical interactions, with applications in nanometrology, sensing, nano-optical control of light and optomechanics. Here, the optically resonant excitation and detection of gigahertz vibrational modes is demonstrated in a nanoscale metasurface array fabricated on a suspended SiC membrane. By designing the main optical and vibrational modes to be those of the individual metamolecules, resonant excitation and detection is achieved making use of direct mechanisms for optomechanical coupling. Ultrafast optical pump-probe studies reveal a multimodal gigahertz vibrational response corresponding to the mechanical modes of the suspended nanoresonators. Wavelength and polarization dependent studies reveal that the excitation and detection of vibrations takes place through the metasurface optical modes. The dielectric metasurface pushes the modulation speed of optomechanical structures closer to their theoretical limits and presents a potential for compact and easily fabricable optical components for photonic applications.

Keywords: Optomechanics, Metasurfaces, Pump-probe, Ultrafast spectroscopy, Metamaterials Nanophotonics

Optomechanics, the use of optically induced forces to control mechanical vibrations, is seeing wide interest for its potential of achieving new quantum entangled states[1], improved optical sensors[2], and on-chip data processing [3, 4]. Rapid progress in fabrication technology is resulting in high quality devices with precisely controlled vibrational and optical resonant response [1, 5-8]. Nanometer-scale mechanical movements can be used to actuate MEMS-type plasmonic and dielectric nanostructures using thermal, electrostatic, magnetic, and optical forces [5, 9-11], with a speed governed by the dimension of the supporting structure and by the dynamics of underlying physical processes, typically in the kHz to few-MHz range.

Metamaterials and metasurfaces offer a platform to engineer the nonlinearity associated with their on-demand optical properties. Nano-optomechanical metasurface arrays are a class of nonlinear photonic metamaterials designed with subwavelength features, 'metamolecules', that mechanically oscillate as a response to optical forces [11-13]. The optomechanical response of the metasurface array (MSA) has been shown to result in giant nonlinear modulation of absorption, transmission and

reflection of incident electromagnetic waves. A. Karvounis *et al.* [11] have demonstrated optomechanical resonances in silicon based MSA with a mechanical frequency response of up to 154 MHz.

Optomechanical driving of resonators at higher frequencies requires a correspondingly reduced mass of the device. Small colloidal nanoparticles and thin nanowires support vibrational modes far into the GHz regime, which are accessible using ultrafast pulsed laser spectroscopy [14, 15] down to the single-particle level [16]. Coherent oscillations in metallic nanostructures are typically driven by ultrafast local heating and impulsive hot electron pressure [17, 18]. Vibrational characteristics of gold nanostructures of various shapes and sizes have been intensively studied [19-26]. Strategical positioning of mechanical oscillators in the optical near-field of a plasmonic nanoantenna has been shown to result in antenna-enhanced readout effects and amplification of small signal response [20]. The coupling of colocalized optical and mechanical resonances in a gold split-ring MSA were recently demonstrated, identifying an acousto-plasmonic coupling induced by the capacitive gap [24].

Here, we demonstrate the multimodal GHz optomechanical resonances in a dielectric, amorphous silicon carbide (3C-SiC) metasurface using ultrafast pump and probe microscopy. The principle of this experiment is shown in Figure 1a. By fabricating the MSAs on a free-standing dielectric membrane, we take advantage of the high stiffness to achieve GHz optomechanical modulation [27]. Resonant excitation through the optical forces associated with the MSA optical resonances is achieved, as well as wavelength and polarization sensitive detection indicative of an acousto-optic metasurface enhanced response. Unlike plasmonic based nanoresonators, where excitation of mechanical oscillations relies on indirect mechanisms involving excitation of a hot electron plasma, acoustic phonons, or surface plasmons [17, 18, 22, 23], dielectric based optomechanical metasurfaces allow direct actuation, control and detection of the mechanical modes by taking advantage of the susceptibility of individual metamolecules to radiation pressure which depends on wavelength and polarization of the excitation source, and which can be appropriately tuned through their subwavelength dimensions. This allows for more flexibility in the range of materials and effects that can be engineered.

The MSA consists of a periodic array of unit cells of 655 nm × 565 nm containing a suspended nano-cantilever with U-shaped slit, milled into a 300 nm thick SiC membrane as shown in Figure 1b. A scanning electron microscopy (SEM) image of the fabricated structure is shown in Figure 1c. The optical response of the MSA was modelled using COMSOL Multiphysics using values of refractive index for the SiC membrane taken from literature[28]. The simulated optical reflection (R), transmission (T) and absorption (A) spectra for a vertically polarized (E_y) and horizontally (E_x) polarized incident beam incident on the periodic MSA are shown in Figure 1d and e. Near-field maps of the z-components of the electric field intensity are presented in Figure 1f for selected wavelengths within the spectral tuning ranges of the pump (1050nm – 1200nm) and probe (780nm – 840nm). Cross sections in the xy and zy planes are shown at locations indicated by the dashed lines, corresponding to the center of the metamolecule for the zy plane and 100 nm below the top surface for the xy plane. The main absorption resonance occurs at 1010 nm for the E_y polarization. For wavelengths above the resonance, the maximum electric near-field intensity is concentrated onto the nanocantilever structure in the metamolecule. At shorter wavelengths (763 and 800 nm), the field intensity is localized mainly on the vertices and the hinge of the nanocantilever.

In addition to inducing spatially distributed electric dipole forces that cause the nanocantilever to mechanically oscillate at specific frequencies[11], the incidence of electromagnetic field with localized absorption at the center of the nanocantilever makes it mechanically susceptible to radiation pressure due to its nanoscale dimensions. Given the structural asymmetry of the metamolecules, it is expected that the optical response is polarization dependent. This is confirmed by differences in the simulated

optical R, T and A spectra in Figure 1d,e. Supporting information Section S7 discusses some of the near-field properties for the horizontal (E_x) polarization.

Experimental R, T and A spectra were obtained using a microspectrophotometer (CRAIC QDI2010), with a 20μm × 20μm sampling aperture via a 15× objective with NA 0.28. The resulting spectra of the MSA are shown in Figures 1g and h for the two polarizations. For E_y polarization (Figure 1g), the dominant absorption feature is in good agreement with the simulations. Effects of inhomogeneous broadening are discussed in Supporting Information Figure S8. Results for E_x polarization shows similar features to the simulations but blueshifted by ~100 nm. In the cases of both E_y and E_x, there is an imperfect agreement between experiments and simulations for the reflection and transmission at shorter wavelengths <900 nm. In the following we focus on understanding the long-wavelength response (orange shaded region in Figure 1d), which is most relevant for our optical pumping scheme and where agreement between simulations and experiments is good. For detection in the 780 nm – 840 nm band, we focus on comparison with experimental linear optical spectra and pump-probe results as presented in Supporting Information Section S3.

The vibrational eigenmodes of the MSA were measured using an ultrafast pump-probe experimental setup as shown in Figure 2a. We used a Ti:sapphire modelocked laser (Coherent Chameleon Ultra II, 80 MHz repetition rate) with optical parametric oscillator (OPO) with a pulse width of 150 fs. The MSA was optically pumped using the OPO signal output tuned from 1050 nm – 1250 nm wavelength, which was modulated at 40 MHz using an acousto-optical pulse picker. The pump was sent through an optical delay stage with a scan range of 3 ns. For the probe we used the fundamental oscillator at wavelengths between 780 nm – 840 nm. The beams were focused onto the MSA to a diffraction-limited waist of around 1 μm using an infrared microscope objective (Mitutoyo) with numerical aperture of 0.5. The pump pulse energy was limited by the efficiency of the pulse picker to around 15 pJ after the objective, resulting in a pump fluence on the sample of up to 0.5 mJ/cm^2. Reflection (R) and transmission (T) intensities were measured using infrared avalanche photodetectors (APD, Thorlabs). The corresponding pump-induced changes ΔR and ΔT were demodulated using an ultrahigh frequency lock-in amplifier (Zurich Instruments) at the modulation frequency of 40 MHz for the pump, while R and T were recovered by demodulating the signal at the 80 MHz probe frequency.

The initial differential responses ΔR/R and ΔT/T, for vertically polarized pump and probe signals, are shown in Figure 2b. Reflection and transmission pairs were measured together in the same scan on the same sample location. Both ΔR/R and ΔT/T exhibit an initial fast response, associated with the ultrafast excitation and picosecond relaxation processes of carriers.[29] The initial ultrafast response is followed by periodic oscillations, over a much longer, nanosecond time duration, which are related to the mechanical eigenmodes of the metamolecules on the MSA as explained below. The fast exponential decay component did not form part of our studies and was effectively removed by subtracting a fit of the signal to a triple exponential decay (described in Supporting Information section S9), to reveal the damped oscillations which are 30 – 50 times weaker than the ultrafast response as shown in Figure 2c. Pulsed excitation does not benefit from enhancement by the mechanical quality factor, as in the case of continuous resonant driving of a single mode, but instead results in a broad spectrum of mechanical modes.[19-26] To reveal the spectrum of modes, a fast Fourier transform (FFT) was carried out on the processed time signals and a >1.5 GHz highpass filter was applied. The results, shown in Figure 2d, reveal distinct modes in the gigahertz range with peak frequencies at 2.33 GHz, 5.33 GHz, 7 GHz, 11 GHz, 11.67 GHz, and 21 GHz. These frequencies are expressed both in the transmission and reflection response with different relative amplitudes. These modes were confirmed by fits of ΔR/R and ΔT/T using damped sinusiodals, as presented in Supporting Information Section S2. While the absolute strength of the fast ΔT/T signal is 2 times larger than the ΔR/R signal, the

individual mechanical components show different ratios, ranging from 3-4 times for the lower frequency modes, to less than 2 times for the two modes at around 11 GHz. This difference indicates differences in the coupling strength of the mechanical modes to the optical reflection and transmission response of the MSA. Reversing the pump and probe wavelengths, i.e. excitation at 800 nm and detection at 1100 nm, did not show a measurable vibrational response (See supporting information section S3).

The mechanical properties of a single metamolecule were simulated with COMSOL Multiphysics using fixed boundary conditions. Other studies have demonstrated the validity of continuum mechanics in nanoscale structures[30, 31]. The single metamolecule model yielded the vibrational modes related to the nanocantilever by itself. In addition, we performed calculations on a 5 × 5 metasurface array in order to elucidate the vibrational modes related to the surrounding structures and mechanical coupling of the nanocantilever (see Supporting Information Section S4). Figure 3a shows the simulated mechanical eigenmodes of the single metamolecule. The color scale indicates the size of the local mechanical displacements of the nanostructure, while the associated deformations are shown scaled to 10% of the geometry. Figure 3b shows the corresponding frequency domain simulation of the mechanical response of the nanocantilever. The vibrational amplitudes were acquired from the surface area integration of the volumetric displacement of the nanocantilever. We directly compare the simulated results with the experimental ΔT/T response (red dashed line in Figure 3b). The first three modes identified in the maps (2.32 GHz, 3.61 GHz and 7.03 GHz) are closely matched to some of the modes that were detected experimentally. The mode at 3.61 GHz is not present in the calculated FFT as it requires an asymmetric load over the cantilever to be effectively excited. This mode appears more strongly for excitation along the E_x polarization as discussed in Supporting Information Figure S9. Based on proximity, we attribute the modes at 12 GHz and 12.03 GHz to the experimentally detected modes at 11 GHz and 11.67 GHz. Because these modes are localized at the bottom vertices and edges of the cantilever, they are particularly sensitive to cantilever length, rounding and fabrication imperfections associated with the corners of the experimental device. The simulation also returned modes at 6.5 GHz and 13.66 GHz which are not prominent in the experimental results. The experimental mode at 5.33 GHz is unaccounted for by the nanocantilever response, but is in fact captured by the 5 × 5 MSA model shown in Figure 3c where we have plotted the vibrational displacement of the support framework with the inset showing the corresponding deformation map. We assume weak coupling between individual metamolecules (see supporting Information Figure S5).

Figure 3d presents the simulated frequency domain distribution of the cantilever displacement components, U_x, U_y and U_z. The modes at 2.33 GHz and 7 GHz are identified as out-of-plane modes of the whole cantilever, which we infer from the dominant role of U_z, and, to a smaller extent U_y. By comparison, U_x is negligible in the former two modes. On the other hand, the prominence of U_z and U_x at 12 GHz results from the inward folding of the bottom vertices of the nanocantilever towards the center axis of the nanocantilever. The mode at 12.3 GHz is dominated by a U_y displacement, with notably small contributions from U_x and U_z. This mode is an in-plane expansion and contraction of the nanocantilever base. The 13.66 GHz mode appears to be a breathing mode of the whole nanocantilever structure, and as such, has contributions from U_x, U_y and U_z in almost equal proportions. The 5.33 GHz mode, shown in the inset of Figure 3d, is dominated by U_x and U_z respectively, which appears as an expansion of the support structure normal to the metamolecule, and an inward twist of the structure in the x-direction.

Using the numerical simulation results, we modelled the wavelength dependence of the time-averaged optical forces acting on the nanocantilever resolved in the XYZ directions, by taking into account the radiation pressure of the photons incident on the nanocantilever of the MSA as well as

the intensity gradient of the local electric field, as described elsewhere[11]. In Figure 4a, the moduli of the net resolved optical forces, represented by F_x, F_y and F_z, are plotted against the wavelength, for incident vertically polarized electric field (E_y). Optical forces up to 0.8 P/c correspond to radiation pressures during the ultrashort laser illumination in the tens of nN range (see Supporting Information section S8). In the spectral range of 1000 nm – 1200 nm, optical forces F_y and F_z, acting in the y and z directions are prominent, while there is practically no contribution from F_x. According to the near-field maps of Figure 1f this range corresponds to the electromagnetic modes where the near-field intensity is concentrated onto the nanocantilever. We compare these optical forces with the experimental pump wavelength dependence of the vibrational eigenmodes for the ΔR/R and ΔT/T signals, respectively shown by the connected spheres of different colors in Figure 4a,b.

The experimentally detected modes at 2.33 GHz (grey), 7 GHz (green) and 11 GHz (orange) both peak in magnitude around 1075 – 1100 nm wavelength, which coincides with the peak wavelength seen for F_z. The modes at 5.33 GHz (brown) and 11.67 GHz (violet) increase further toward 1050 nm wavelength, which is the lower limit of our OPO tuning range. These observations appear qualitatively consistent with the main displacement components in Figure 3d. This agreement is more obvious in the cases of the 2.33 GHz and 11 GHz (12 GHz simulation) modes, which are both dominated by an out-of-plane displacement in the z-direction, as well as the 11.67 GHz (12.3 GHz simulation) which is dominated by a y-direction displacement. The 5.33 GHz mode requires a flexing of the beams in the direction normal to the metasurface, therefore it will take a compressive lateral force in the y-direction to induce such a deformation. As such, we believe the pump wavelength dependent results are consistent with the results from our mechanical simulation. These results demonstrate that the individual vibrational modes of the metamolecule can be selectively tuned by changing the wavelength of the pump signal. Additional results showing also the strong dependence on the wavelength of the probe are presented in Supporting Information Section S3.

Next to wavelength dependence, we study in Figure 4c-e the polarization dependence of the vibrational response for both pump and probe for ΔR/R and ΔT/T. Keeping the probe polarization fixed along E_y, we respectively measured the response for pump polarization along y ($E_{y\text{-}y}$) and along x ($E_{x\text{-}y}$). We observe similar multimodal oscillations in both cases, which shows that the frequencies of the mechanical resonances do not strongly depend on the pump polarization. The relative ratios of the different vibrational modes are changed when changing the pump polarization, showing a stronger excitation of the fundamental mechanical mode for pumping along E_x, accompanied with a reduction in the higher frequency component at 11 GHz. The observed variations of the 5.33 GHz vibrational mode in all our experiments appear less systematic and may be attributed to higher sensitivity of the frame modes to very small variations in alignment. Next, we changed the polarization of the probe beam along x, while keeping the pump polarization along y-direction ($E_{y\text{-}x}$). In this configuration, the presence of the mechanical modes in ΔR/R is much less strong. The dependence of the detected signal on orientation of the probe polarization shows that the acousto-optic readout takes place through the polarization-dependent MSA resonances. $E_{x\text{-}x}$ (not shown here) yields the same result as $E_{y\text{-}x}$. As such, the polarization dependence information of the metamolecules is contained in the three spectra presented in Figure 4c.

The different sets of results presented above shows small but noticeable differences in exact experimental frequencies, the number of individual resonance modes in the spectrum and their relative amplitudes in the pump-probe response. These differences suggest an experimental variation of parameters, possibly related to local fabrication imperfections and sample inhomogeneity. This is explored in Figure 5 presenting a set of pump-probe measurements over a 6 μm × 6 μm area taken in the center region of the MSA. The corresponding time-domain plots and FFTs for each of the

indicated points are shown in Figure 5b and c for ΔR/R (ΔT/T shown in Supporting Information Figure S8). Variations in both the center frequencies as well as relative intensities of all the mechanical modes are observed, with generally unsystematic behavior of the 5.33 GHz frame mode. Overall, the mechanical modes of the MSA appear sensitive to local fabrication inhomogeneities across the surface. More detailed spectroscopic data in Supporting Information Figure S8 confirm that local variations are present also in the linear optical response of the MSA.

In conclusion, gigahertz vibrational resonances were demonstrated in a SiC dielectric meta-surface array (MSA). The dielectric MSA provides a direct mechanism for optical excitation through light forces and provides tunability through the wavelength and polarization of the optical pump. Numerical simulations and optical experiments confirm effective driving of cantilever modes in spectral bands around 2, 5, 7, 11 and 21 GHz. The direction-resolved optical forces acting on the nanocantilever were numerically evaluated with respect to wavelength and were shown to result in different dependencies for different modes. We find that, while the vibrational modes are impartial to the polarization of the driving optical force, the reflection property of the nanocantilever in the spectral detection band is most polarization selective. The domain of optical metasurfaces with vibrationally resonant unit cells in the gigahertz range holds promise for new applications in nonlinear optomechanics and our first characterizations invite further exploration. Future work will explore reduction of optical loss, regimes of higher vibrational amplitudes achievable through stronger and resonant pumping, precise control over resonant vibrational characteristics, and applications in nonlinear, time-dependent or active metasurfaces.

Supporting information

The supporting information is available free of charge via the internet at: https://pubs.acs.org/.

- Effects of ambient pressure on vibrational modes, multi-damped oscillator model, probe signal analysis, COMSOL mechanical simulation models, comparison between Si and SiC metamolecules, 7 GHz mode analysis, polarization dependence of hyperspectral maps, optical force estimation, multi-exponential treatment of electronic excitation response.

Acknowledgements

This work was supported by the Engineering and Physical Sciences Research Council (Grants No. EP/S008764/1, EP/M009122/1 and EP/ T02643X/1) and the Singapore Ministry of Education (Grant No. MOE2016-T3-1-006). HJS acknowledges support by the Leverhulme Trust through project RPG-2018-251. All data supporting this study are openly available from the University of Southampton repository (DOI: 10.5258/SOTON/D1812).

References

1. Aspelmeyer, M.; Kippenberg, T. J.; Marquardt, F., Cavity optomechanics. *Rev. Mod. Phys.* **2014,** *86* (4), 1391-1452.
2. Metcalfe, M., Applications of cavity optomechanics. *Appl. Phys. Rev.* **2014,** *1* (3), 031105.
3. Van Thourhout, D.; Roels, J., Optomechanical device actuation through the optical gradient force. *Nat. Photon.* **2010,** *4* (4), 211-217.
4. Eggleton, B. J.; Poulton, C. G.; Rakich, P. T.; Steel, M. J.; Bahl, G., Brillouin integrated photonics. *Nat. Photon.* **2019,** *13* (10), 664-677.
5. Thijssen, R.; Kippenberg, T. J.; Polman, A.; Verhagen, E., Plasmomechanical Resonators Based on Dimer Nanoantennas. *Nano Lett.* **2015,** *15* (6), 3971-3976.

6. Eichenfield, M.; Chan, J.; Camacho, R. M.; Vahala, K. J.; Painter, O., Optomechanical crystals. *Natur* **2009,** *462* (7269), 78-82.
7. Lanzillotti-Kimura, N. D.; Fainstein, A.; Huynh, A.; Perrin, B.; Jusserand, B.; Miard, A.; Lemaitre, A., Coherent generation of acoustic phonons in an optical microcavity. *Phys. Rev. Lett.* **2007,** *99* (21), 217405.
8. Meenehan, S. M.; Cohen, J. D.; MacCabe, G. S.; Marsili, F.; Shaw, M. D.; Painter, O., Pulsed Excitation Dynamics of an Optomechanical Crystal Resonator near Its Quantum Ground State of Motion. *Phys. Rev. X* **2015,** *5* (4), 041002.
9. Zheludev, N. I.; Plum, E., Reconfigurable nanomechanical photonic metamaterials. *Nat. Nanotechnol.* **2016,** *11* (1), 16-22.
10. Holsteen, A. L.; Raza, S.; Fan, P. Y.; Kik, P. G.; Brongersma, M. L., Purcell effect for active tuning of light scattering from semiconductor optical antennas. *Science* **2017,** *358* (6369), 1407-1410.
11. Karvounis, A.; Ou, J.-Y.; Wu, W.; MacDonald, K. F.; Zheludev, N. I., Nano-optomechanical nonlinear dielectric metamaterials. *Appl. Phys. Lett.* **2015,** *107* (19), 191110.
12. Zhang, J.; MacDonald, K. F.; Zheludev, N. I., Nonlinear dielectric optomechanical metamaterials. *Light Sci. Appl.* **2013,** *2* (8), e96-e96.
13. Ou, J.-Y.; Plum, E.; Zhang, J.; Zheludev, N. I., Giant Nonlinearity of an Optically Reconfigurable Plasmonic Metamaterial. *Adv. Mater.* **2016,** *28* (4), 729-733.
14. Hartland, G. V., Optical Studies of Dynamics in Noble Metal Nanostructures. *Chem. Rev.* **2011,** *111* (6), 3858-3887.
15. Beane, G.; Devkota, T.; Brown, B. S.; Hartland, G. V., Ultrafast measurements of the dynamics of single nanostructures: a review. *Rep. Prog. Phys.* **2019,** *82* (1), 016401.
16. van Dijk, M. A.; Lippitz, M.; Orrit, M., Detection of acoustic oscillations of single gold nanospheres by time-resolved interferometry. *Phys. Rev. Lett.* **2005,** *95* (26).
17. Wright, O. B., Ultrafast Nonequilibrium Stress Generation in Gold and Silver. *Phys. Rev. B* **1994,** *49* (14), 9985-9988.
18. Perner, M.; Gresillon, S.; Marz, J.; von Plessen, G.; Feldmann, J.; Porstendorfer, J.; Berg, K. J.; Berg, G., Observation of hot-electron pressure in the vibration dynamics of metal nanoparticles. *Phys. Rev. Lett.* **2000,** *85* (4), 792-795.
19. Antonelli, G. A.; Maris, H. J.; Malhotra, S. G.; Harper, J. M. E., Picosecond ultrasonics study of the vibrational modes of a nanostructure. *J. Appl. Phys.* **2002,** *91* (5), 3261-3267.
20. Schumacher, T.; Kratzer, K.; Molnar, D.; Hentschel, M.; Giessen, H.; Lippitz, M., Nanoantenna-enhanced ultrafast nonlinear spectroscopy of a single gold nanoparticle. *Nat. Commun.* **2011,** *2*, 333.
21. Kelf, T. A.; Hoshii, W.; Otsuka, P. H.; Sakuma, H.; Veres, I. A.; Cole, R. M.; Mahajan, S.; J Baumberg, J.; Tomoda, M.; Matsuda, O.; Wright, O. B., Mapping gigahertz vibrations in a plasmonic–phononic crystal. *New J. Phys* **2013,** *15* (2), 023013.
22. O'Brien, K.; Lanzillotti-Kimura, N. D.; Rho, J.; Suchowski, H.; Yin, X. B.; Zhang, X., Ultrafast acousto-plasmonic control and sensing in complex nanostructures. *Nat. Commun.* **2014,** *5*, 4042.
23. Ulbricht, R.; Sakuma, H.; Imade, Y.; Otsuka, P. H.; Tomoda, M.; Matsuda, O.; Kim, H.; Park, G.-W.; Wright, O. B., Elucidating gigahertz acoustic modulation of extraordinary optical transmission through a two-dimensional array of nano-holes. *Appl. Phys. Lett.* **2017,** *110* (9), 091910.
24. Imade, Y.; Ulbricht, R.; Tomoda, M.; Matsuda, O.; Seniutinas, G.; Juodkazis, S.; Wright, O. B., Gigahertz Optomechanical Modulation by Split-Ring-Resonator Nanophotonic Meta-Atom Arrays. *Nano Lett.* **2017,** *17* (11), 6684-6689.
25. Yi, C. Y.; Dongare, P. D.; Su, M. N.; Wang, W. X.; Chakraborty, D.; Wen, F. F.; Chang, W. S.; Sader, J. E.; Nordlander, P.; Halas, N. J.; Link, S., Vibrational coupling in plasmonic molecules. *Proc. Natl. Acad. Sci. U.S.A.* **2017,** *114* (44), 11621-11626.

26. Medeghini, F.; Crut, A.; Gandolfi, M.; Rossella, F.; Maioli, P.; Vallee, F.; Banfi, F.; Del Fatti, N., Controlling the Quality Factor of a Single Acoustic Nanoresonator by Tuning its Morphology. *Nano Lett.* **2018,** *18* (8), 5159-5166.
27. Mitin, V. V.; Kochelap, V. A.; Stroscio, M. A., Nanostructure devices. In *Introduction to Nanoelectronics: Science, Nanotechnology, Engineering, and Applications*, Cambridge University Press: Cambridge, 2007; pp 242-322.
28. Wang, S.; Zhan, M.; Wang, G.; Xuan, H.; Zhang, W.; Liu, C.; Xu, C.; Liu, Y.; Wei, Z.; Chen, X., 4H-SiC: a new nonlinear material for midinfrared lasers. *Laser & Photonics Reviews* **2013,** *7* (5), 831-838.
29. Fang, Y.; Nie, Y.; Wu, X.; Yang, J.; Chen, Y.; Wang, Y.; Wu, Q.; Song, Y., Excitation wavelength-dependent carrier dynamics in n-type and semi-insulating 6H-SiC using ultrafast transient absorption spectroscopy. *J. Appl. Phys.* **2019,** *125* (23), 235703.
30. Ansari, R.; Rouhi, S.; Aryayi, M., Nanoscale finite element models for vibrations of single-walled carbon nanotubes: atomistic versus continuum. *Applied Mathematics and Mechanics-English Edition* **2013,** *34* (10), 1187-1200.
31. Govindjee, S.; Sackman, J. L., On the use of continuum mechanics to estimate the properties of nanotubes. *Solid State Commun.* **1999,** *110* (4), 227-230.

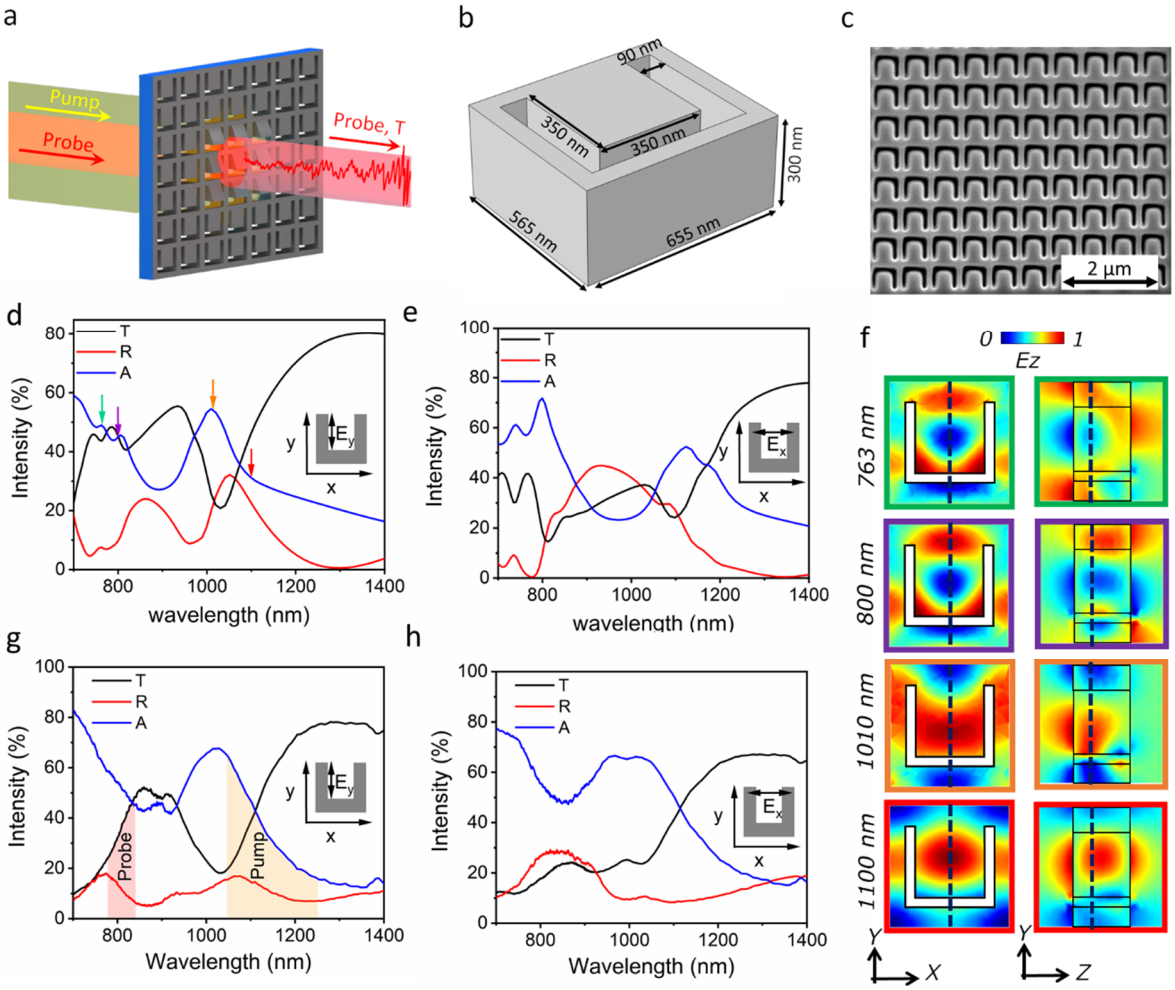

Figure 1 (a) Concept image showing multimodal vibrational response of the probe signal through optical excitation of the MSA. (b) Schematic showing the dimensions of a single metamolecule. (c) SEM image of the fabricated MSA showing the "U" shaped metamolecules. (d, e) Simulated transmission (T), reflection (R) and absorption (A) spectra of a metamolecule in the SiC MSA in vertical and horizontal polarization, respectively. (f) Simulated normalized electric field intensity distribution in the xy and zy directions of the metamolecule at indicated wavelengths in vertical polarization. (g, h) Average experimental transmission (T), reflection (R) and absorption (A) spectra of the metamaterial surface array in vertical and horizontal polarization, respectively.

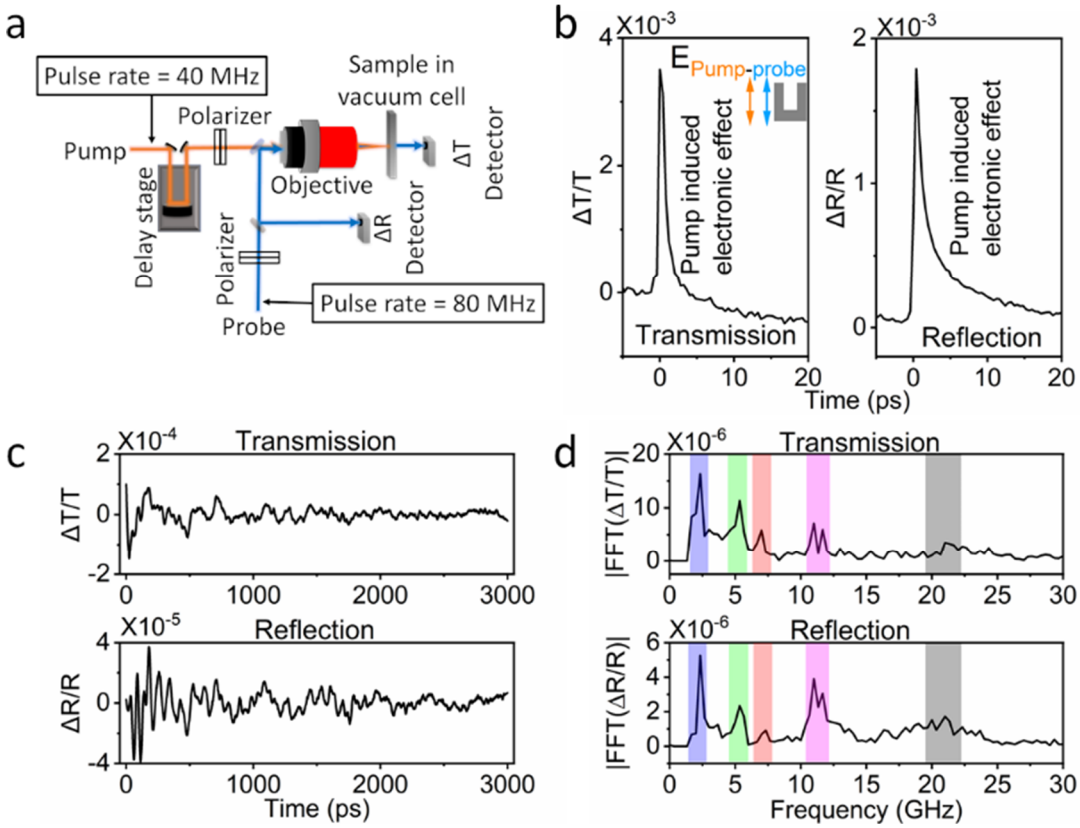

Figure 2 (a) Schematic showing the ultrafast pump-probe setup. (b) Normalized transmission (ΔT/T) and reflection (ΔR/R) intensity response showing the electronic response of SiC. (c) Smoothened optomechanical response of the metamolecules in transmission and reflection modes after removal of the electronic effect using a tri-exponential function curve fit. (d) Fast-Fourier transform (FFT) spectra of the transmission and reflection optomechanical responses showing the vibrational modes of the optically activated metamolecules.

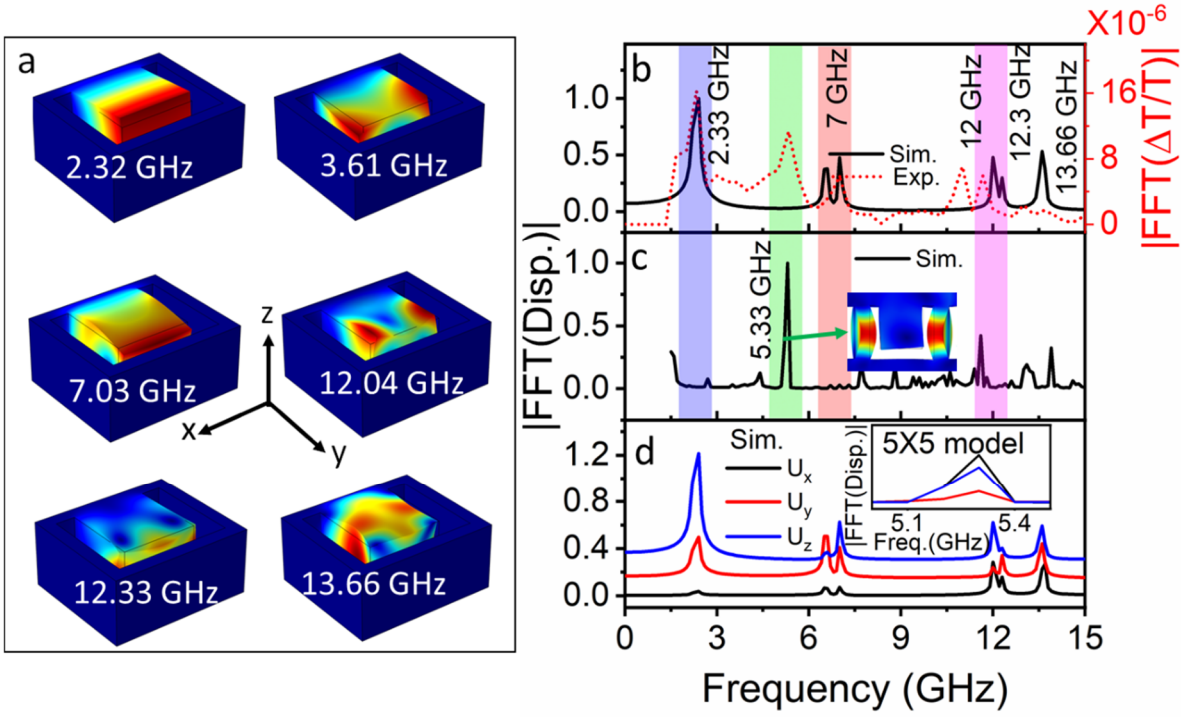

Figure 3 (a) Simulated mechanical eigenmodes of a single metamolecule at selected frequencies. (b) Simulated frequency domain plot of a single metamolecule, showing the normalized mechanical displacement response of the cantilever (solid black). The experimental |FFT(ΔT/T)| (dotted red plot) is superimposed for reference. (c) Simulated frequency domain plot of a 5 × 5 metasurface array, showing the normalized mechanical displacement response of the bridges enclosing the cantilever. A single metamolecule showing the vibration mode of the bridges at 5.33 GHz is shown in the inset. (d) Simulated frequency domain plot of the directional components of mechanical displacement for the nanocantilever of a single metamolecule (stacked for clarity) and (inset) The directional components of the support structures of a simulated 5 × 5 MSA at 5.33 GHz.

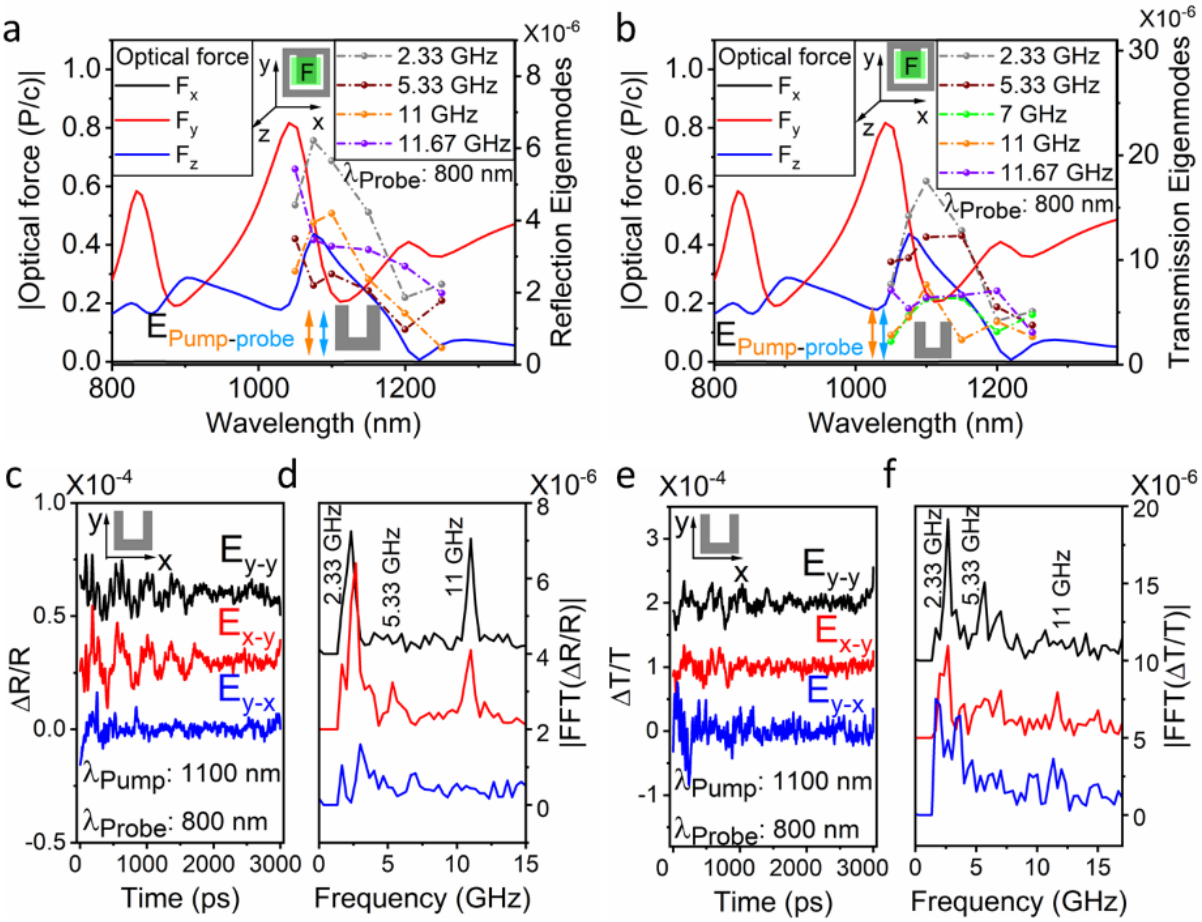

Figure 4 (a,b) Wavelength dependence of the moduli of the optical force magnitudes (left y-axis) acting on the nanocantilever in xyz directions superimposed on the pump wavelength dependence of the optomechanical magnitudes in reflection mode (right y-axis), for reflection (a) and transmission (b) eigenmodes. (c-f) Time-domain (c,e) and frequency-domain (d,f) plots of the optomechanical responses of the nanocantilever at vertical-vertical (black line), horizontal- vertical (red line) and vertical-horizontal (blue line) pump-probe polarizations for reflection (c,d) and transmission (e,f). The plots are vertically stacked for clarity.

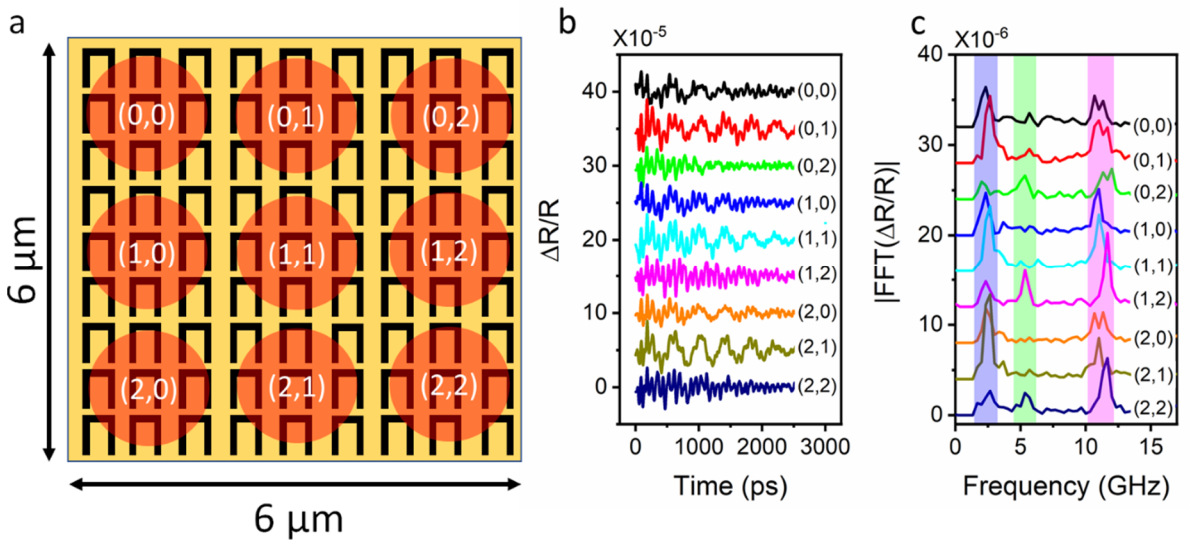

Figure 5 (a) Illustration of the aerial pump-probe scan of the MSA with labelled scan regions. (b) Time-domain plots corresponding to the indicated scan regions stacked for clarity. (c) FFT spectra corresponding to the labelled scan regions, stacked for clarity. Polarization of pump and probe was taken along the y-direction.

TOC Graphic:

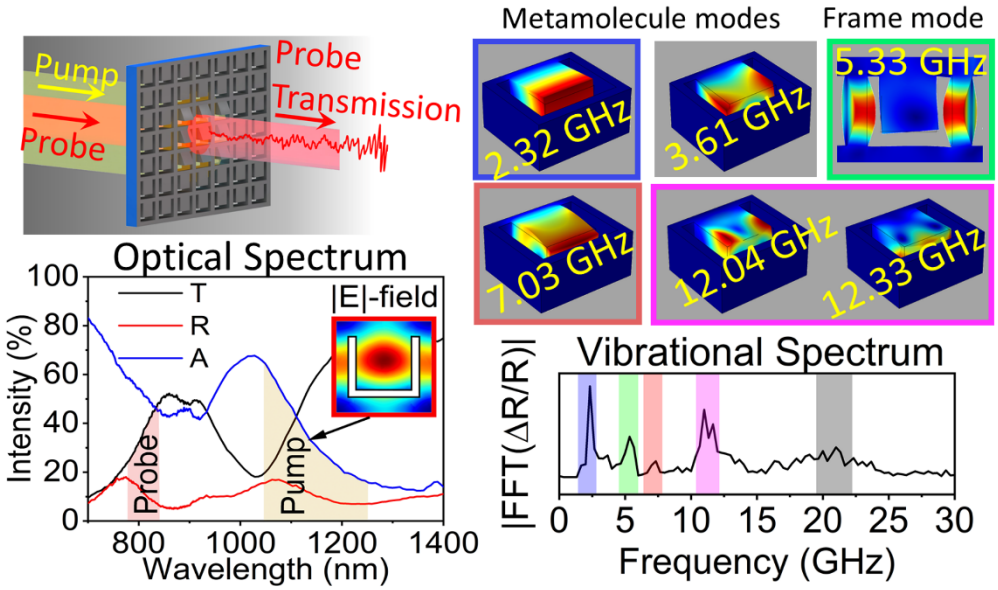
Pump
Probe
Probe
Transmission
Optical Spectrum
100
80
60
40
20
0
Intensity (%)
T
R
A
|E|-field
Probe
Pump
800
1000
1200
1400
Wavelength (nm)
Metamolecule modes
Frame mode
2.32 GHz
3.61 GHz
5.33 GHz
7.03 GHz
12.04 GHz
12.33 GHz
Vibrational Spectrum
|FFT(ΔR/R)|
0
5
10
15
20
25
30
Frequency (GHz)